Two-photon spectroscopy of excitons with entangled photons

Frank Schlawin[1,2,a)] and Shaul Mukamel[1,b)]
[1]*Department of Chemistry, University of California, Irvine, California 92697-2025, USA*
[2]*Physikalisches Institut, Albert-Ludwigs-Universität Freiburg, Hermann-Herder-Straße 3, 79108 Freiburg, Germany*

(Received 26 September 2013; accepted 2 December 2013; published online 30 December 2013)

The utility of quantum light as a spectroscopic tool is demonstrated for frequency-dispersed pump-probe, integrated pump-probe, and two-photon fluorescence signals which show Ramsey fringes. Simulations of the frequency-dispersed transmission of a broadband pulse of entangled photons interacting with a three-level model of matter reveal how the non-classical time-bandwidth properties of entangled photons can be used to disentangle congested spectra, and reveal otherwise unresolved features. Quantum light effects are most pronounced at weak intensities when entangled photon pairs are well separated, and are gradually diminished at higher intensities when different photon pairs overlap. © *2013 AIP Publishing LLC*. [http://dx.doi.org/10.1063/1.4848739]

I. INTRODUCTION

In the past 20 years, nonlinear optical spectroscopy has evolved into an indispensable tool for probing non-equilibrium dynamics in many-body systems such as photosynthetic complexes,[1–4] semiconductors,[5,6] and strongly correlated materials.[7–9] The various theoretical concepts developed in these areas call for the design of new experiments to test the underlying dynamics. One promising new resource for nonlinear spectroscopy lies in the use of quantum properties of the light, where quantum effects such as entanglement can be exploited to manipulate optical signals.

In this paper, we use a diagrammatic superoperator approach to simulate frequency-dispersed transmission measurements of broadband entangled photon pulses in a three-level system. The technique can be applied to bulk as well as single molecules. Most single molecule experiments use fluorescence detection, but direct absorption had been reported as well.[10–12] All of these measurements depend on the four-point field correlation function, which is responsible for the many photon correlation effects usually attributed to entangled light such as dispersion cancellation[13] or sub-wavelength diffraction.[14] Therefore, we can expect to see signatures of the quantum nature of the light in such signals. The four-point correlation function scales quadratically in the pump intensity for classical laser pulses, but linearly for entangled photons. This favorable intensity scaling[15–18] has been demonstrated experimentally in various systems, and allows to perform measurements at low intensities, avoiding damage to the sample. Moreover, the non-classical time-bandwidth properties of entangled photon pairs[19–21] provide unconventional observation windows, and can be used to selectively excite specific two-exciton states[21] or specific vibrational states,[22,23] and control population transport.[24] New control parameters of quantum light can be varied to create novel two-dimensional correlation plots.[25,26]

Another promising technique involves the detection of fluorescence signals after excitation by quantum light or using phase cycling.[27–29] It has been shown by Qu and Agarwal[30] that entangled beams can also give rise to Ramsey fringes with twice the frequency resolution of classical light in two-photon counting experiments. Our formalism generalizes these results to describe arbitrary pulse shapes rather than square pulses, and more general matter systems. Similar results have been obtained for coherent signals with heterodyne detection.[31]

II. FREQUENCY-DISPERSED PUMP-PROBE SIGNALS

We consider the setup and the three-level system as sketched in Figure 1. Two entangled photon beams E_1 and E_2 created by parametric down-conversion are directed onto the sample. The change in transmission of field E_2 at frequency ω due to the interaction with matter is recorded. Similar setups have been used in Ref. 18, where count rates on the order of 10^7 photons/s have been reported. The frequency-dispersed detection proposed here is expected to yield comparable but somewhat lower count rates.

The signal is given by

$$S(\Gamma;\omega,\delta t)=\frac{2}{\hbar}\Im\langle E_2^{\dagger}(\omega)P^{(3)}(\omega)\rangle, \tag{1}$$

where the third-order polarizability

$$P^{(3)}(\omega)=\int dt e^{i\omega t}P^{(3)}(t) \tag{2}$$

is induced by the interaction of the matter system with the light field. The set of control parameters Γ includes the pump pulse frequency ω_p and its bandwidth σ_p, the central frequencies of the downconverted beams ω_1 and ω_2, their entanglement time T specifying their bandwidths, and the amplitude of the pump pulse α as discussed in Ref. 32. δt is a variable delay. Expanding Eq. (1) to third order in matter-field interactions, we obtain the diagrams of Figure 2. Diagram rules are given in Ref. 33. Diagrams (a) and (b) in Fig. 2 pass through the doubly excited state $|f\rangle$, we thus denote them double quantum coherence (DQC) pathways,

a)Electronic mail: Frank.Schlawin@physik.uni-freiburg.de
b)Electronic mail: smukamel@uci.edu

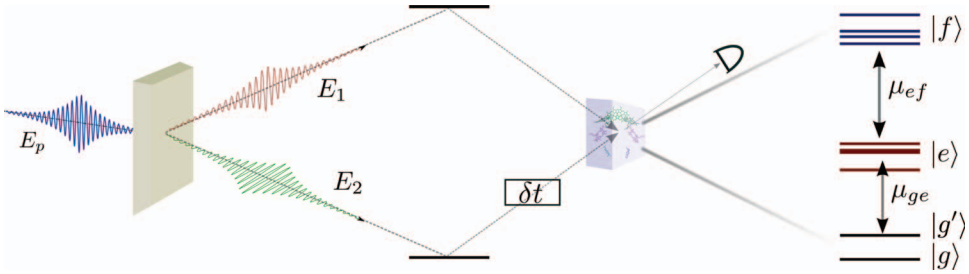

FIG. 1. Left: Setup for the pump-probe experiment with entangled photons. The two beams are generated by parametric down-conversion and interact with the sample modelled as a three-level system (right). The transmission of beam 2, which delayed by δt, is recorded. Right: Our three three-level system.

$$S_a(\Gamma;\omega,\delta t) = \frac{2}{\hbar}\sum_{e,e',f}\Im\frac{i^3\mu_{fe'}\mu_{e'g}}{\omega-\omega_{e'g}+i\gamma_{e'}}\left(\frac{-i}{\hbar}\right)^3\int\frac{d\omega_a}{2\pi}\int\frac{d\omega_b}{2\pi}\frac{\mu_{ge}}{\omega_a-\omega_{eg}+i\gamma_e}\frac{\mu_{ef}}{\omega_a+\omega_b-\omega_{fg}+i\gamma_f}$$
$$\times[\langle E_2^\dagger(\omega)E_1^\dagger(\omega_a+\omega_b-\omega)E_2(\omega_b)E_1(\omega_a)\rangle e^{i(\omega+\omega_a-\omega_{eg}-\omega_{e'g}+i2\gamma_e)\delta t}$$
$$+\langle E_2^\dagger(\omega)E_1^\dagger(\omega_a+\omega_b-\omega)E_1(\omega_b)E_2(\omega_a)\rangle e^{i(\omega-\omega_{e'g}+i\gamma_e)\delta t}], \tag{3}$$

$$S_b(\Gamma;\omega,\delta t) = \frac{2}{\hbar}\sum_{e,e',f}\Im i^3\left(\frac{-i}{\hbar}\right)^3\int\frac{d\omega_a}{2\pi}\int\frac{d\omega_b}{2\pi}\frac{\mu_{ge}}{\omega_a-\omega_{eg}+i\gamma_e}$$
$$\times\frac{\mu_{ef}}{\omega_a+\omega_b-\omega_{fg}+i\gamma_f}\frac{\mu_{fe'}\mu_{e'g}}{\omega_a+\omega_b-\omega-\omega_{e'g}-i\gamma_{e'}}$$
$$\times[\langle E_1^\dagger(\omega_a+\omega_b-\omega)E_2^\dagger(\omega)E_2(\omega_b)E_1(\omega_a)\rangle e^{i(\omega-\omega_b-\omega_{ee'}+i2\gamma_e)\delta t}$$
$$+\langle E_1^\dagger(\omega_a+\omega_b-\omega)E_2^\dagger(\omega)E_1(\omega_b)E_2(\omega_a)\rangle e^{i(\omega-\omega_{fe'}+i(\gamma_e+\gamma_f))\delta t}]. \tag{4}$$

Diagrams (c) and (d) in Fig. 2 pass through a ground state vibrational resonance $|g'\rangle$ after two interactions. We thus denote them Raman pathways,

$$S_c(\Gamma;\omega,\delta t) = \frac{2}{\hbar}\sum_{e,e',g'}\Im\frac{i^3\mu_{g'e'}\mu_{e'g}}{\omega-\omega_{e'g}+i\gamma_{e'}}\left(\frac{-i}{\hbar}\right)^3\int\frac{d\omega_a}{2\pi}\int\frac{d\omega_b}{2\pi}\frac{\mu_{ge}}{\omega_a-\omega_{eg}+i\gamma_e}\frac{\mu_{eg'}}{\omega_a-\omega_b-\omega_{g'g}+i\gamma_g}$$
$$\times[\langle E_2^\dagger(\omega)E_2(\omega_a+\omega_b-\omega)E_1^\dagger(\omega_b)E_1(\omega_a)\rangle e^{i(\omega_a-\omega_b-\omega_{g'g}+i\gamma_g)\delta t}$$
$$+\langle E_2^\dagger(\omega)E_1(\omega_a+\omega_b-\omega)E_1^\dagger(\omega_b)E_2(\omega_a)\rangle e^{i(\omega-\omega_{e'g}+i\gamma_e)\delta t}], \tag{5}$$

$$S_d(\Gamma;\omega,\delta t) = \frac{2}{\hbar}\sum_{e,e',g'}\Im i^3\left(\frac{-i}{\hbar}\right)^3\int\frac{d\omega_a}{2\pi}\int\frac{d\omega_b}{2\pi}\frac{\mu_{ge}}{\omega_a-\omega_{eg}+i\gamma_e}$$
$$\times\frac{\mu_{eg'}}{\omega_a-\omega-\omega_{g'g}-i\gamma_g}\frac{\mu_{g'e'}\mu_{e'g}}{\omega_a+\omega_b-\omega-\omega_{e'g}-i\gamma_e}$$
$$\times[\langle E_1^\dagger(\omega_a+\omega_b-\omega)E_1(\omega_b)E_2^\dagger(\omega)E_2(\omega_a)\rangle e^{i(\omega-\omega_a+\omega_{g'g}+i\gamma_g)\delta t}$$
$$+\langle E_1^\dagger(\omega_a+\omega_b-\omega)E_2(\omega_b)E_2^\dagger(\omega)E_1(\omega_a)\rangle e^{i(\omega-\omega_b-\omega_{ee'}+i2\gamma_e)\delta t}]. \tag{6}$$

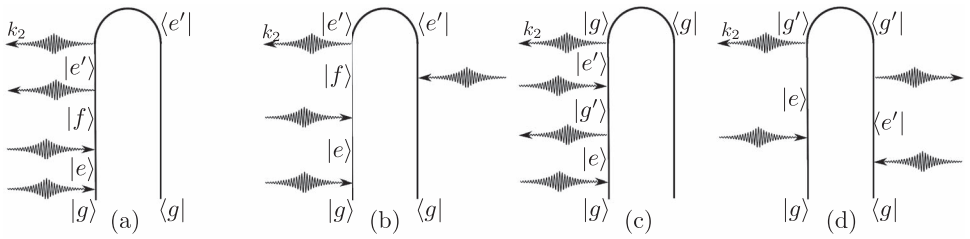

FIG. 2. Loop diagrams for the various pathways of the pump-probe signal. Unlabelled arrows represent the total field $E_1 + E_2$. Diagrams (a) and (b) represent double quantum coherence (DQC) pathways, and diagrams (c) and (d) are Raman pathways.

Our terminology is based on following the field along the loop. The DQC contributions contain $\langle E^\dagger E^\dagger EE\rangle$ field correlation functions, whereas the Raman terms have $\langle E^\dagger EE^\dagger E\rangle$. We are using a frequency-domain representation that yields more compact expressions for the signals. Equations (3)–(6) will be used in the following simulations.

III. SIMULATIONS OF DQC-SIGNALS

We use the squeezed light model as described in the Appendix. This model corresponds to parametric downconversion as illustrated in Figure 1. A pump photon with frequency ω_p' is downconverted into two, signal and idler, photons with frequencies ω_1' and ω_2', such that $\omega_p' = \omega_1' + \omega_2'$. The bandwidth of the two beams is characterized by the entanglement time T, and it can greatly exceed the bandwidth of the pump pulse.[25] In this case, the two photons are said to be frequency-time entangled, since their sum is distributed according to the pump bandwidth. The two central frequencies of the downconverted beams can be varied experimentally by adjusting the phase matching conditions inside the nonlinear crystal. We will restrict our discussion to degenerate downconversion, i.e., the central frequencies of the two beams coincide, $\omega_1 = \omega_2 = \omega_p/2$.

We first simulate the DQC-pathways. Using Eq. (A4), we have evaluated the frequency integrations in Eqs. (3) and (4) numerically by sampling ± 10 standard deviations of the pump around the central frequencies of the two pulses.

We consider the Frenkel exciton model system shown in Figure 1, consisting of two single-exciton states with energies $e_1 = 10\,000\ \mathrm{cm}^{-1}$ and $e_2 = 11\,000\ \mathrm{cm}^{-1}$, and two two-exciton states with $f_1 = 20\,000\ \mathrm{cm}^{-1}$ and $f_2 = 21\,500\ \mathrm{cm}^{-1}$. The dipole moments connecting the states are taken to be the identical. All transitions are broadened by a dephasing rate $\gamma = 100\ \mathrm{cm}^{-1}$. The system shows one harmonic, one weakly anharmonic one, and two strongly anharmonic two-exciton transitions.

Nonlinear optical signals are created by anharmonicities of matter.[34,35] If the two-exciton states are all given by the sum the single-exciton energies, i.e., $\epsilon_f = \epsilon_{e_i} + \epsilon_{e_j}\ \forall f$, the signals are cancelled by destructive interference. Only interactions between the single excitons give rise to a nonvanishing signal. The diagrams are normalized such that their maximal value is ± 1. The impact of the anharmonicity can be read off the signal in the left panel in Figure 3 (top row). For $\omega_p = \omega_{f_2 g}$ we observe several peaks along the horizontal ω-axis. At $\omega = 10\,500\ \mathrm{cm}^{-1}$, an absorptive peak appears corresponding to the $e_2 \leftrightarrow f_2$-transition, which is weakly

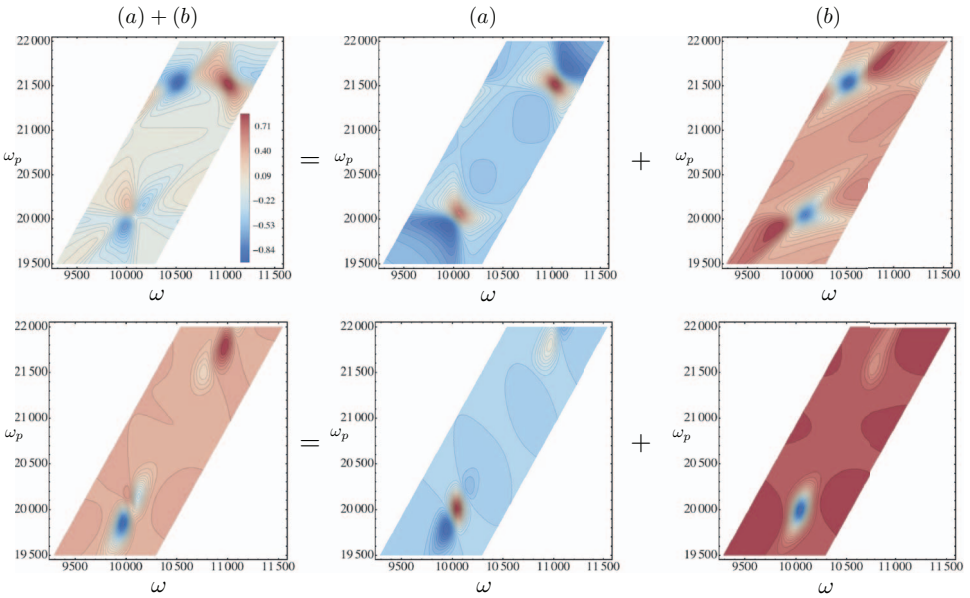

FIG. 3. Top row: The DQC-signal [Eqs. (3) and (4)] is plotted vs the pump frequency ω_p and the dispersed frequency ω for entangled photons. The three panels depict diagrams (a) and (b) of Fig. 2 and their sum as marked. Bottom row: Same as top row, but for excitation by classical laser pulses.

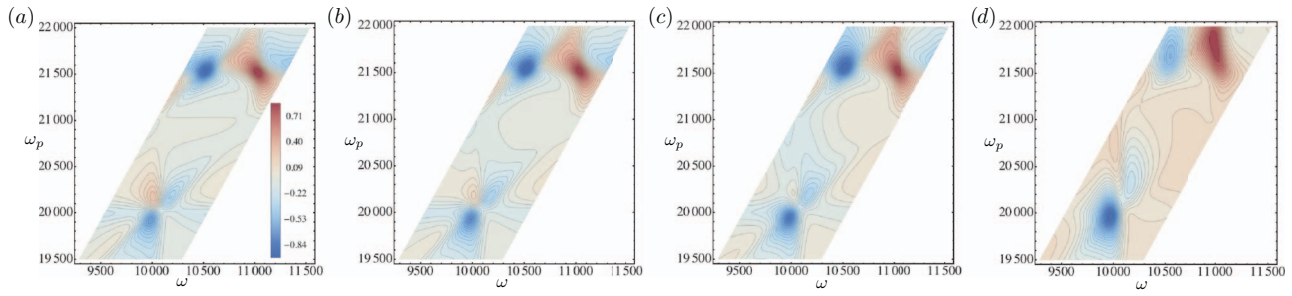

FIG. 4. The DQC-pathways (Eqs. (3) and (4)) are plotted vs the pump frequency ω_p and the dispersed frequency ω with different pump amplitudes (a) $\alpha = 0.0001$, (b) $\alpha = 0.005$, (c) $\alpha = 0.01$, and (d) $\alpha = 0.1$. As α is increased the light state changes from twin photons to squeezed light.

anharmonic. At $\omega = 11\ 500\ \text{cm}^{-1}$, the strongly anharmonic $e_1 \leftrightarrow f_2$-transition (only shown partially) creates a dispersive resonance. In contrast, on resonance with the harmonic two exciton-state f_1 at $\omega_p = 20\ 000\ \text{cm}^{-1}$, the resonances are weaker, even though their dipole moments have the same strength. In the depicted ω-regime, only the resonant transition $e_1 \leftrightarrow f_1$ can be observed. As can be seen from the other two panels corresponding to diagrams (a) and (b) in Fig. 3, respectively, it is eliminated by destructive interference of the two diagrams. Diagram (a) shows a negative resonance at this point, and diagram (b) a positive one, such that their sum only yields a small residual signal.

For comparison, in the bottom row we depict the DQC-signal for excitation by a classical laser pulses, where the four-point correlation function in Eqs. (3) and (4) factorizes into a product of laser pulse amplitudes,

$$\langle E^\dagger(\omega_a')E^\dagger(\omega_b')E(\omega_b)E(\omega_a)\rangle = E^*(\omega_a')E^*(\omega_b')E(\omega_b)E(\omega_a), \tag{7}$$

and we used the Gaussian field envelope

$$E(\omega) = \exp\left[-\frac{(\omega-\omega_p/2)}{2\sigma^2}\right]. \tag{8}$$

We chose the bandwidth σ to coincide with the bandwidth σ_p of the pump pulse which creates the entangled pair. This ensures the same frequency resolution when varying ω_p as in the case of entangled photons, such that the peak structures can be readily compared. The signal shows the same destructive interference as in the quantum case. However, it is peaked when the beam is on resonance with a single-exciton transition, i.e., at 20 000 and 22 000 cm^{-1}. Only diagram (b) shows a two-exciton resonance at 21 500 cm^{-1} [right panel in the bottom row], but it is partially masked by the stronger resonance of diagram (a) at 22 000 cm^{-1}.

Figure 4 illustrates how the non-classical properties of entangled beams are degraded, as the pump intensity $|\alpha|^2$ is increased, and different entangled pairs overlap in time. Signals involving photons belonging to different pairs are classical. Figure 4(a) shows again the same twin-photon dominated signal, where the anharmonic two-exciton state is much brighter than the harmonic one. In panel (c), the latter peaks become stronger due to incoherent contributions on resonance with the $g \rightarrow e_1$-transition, and for even stronger pump intensities [panel (d)] the signal is dominated by single photon resonances $g \rightarrow e_{1,2}$ at $\omega = 10\ 000$ and $11\ 000\ \text{cm}^{-1}$, respectively.

To rationalize this dependence on the pump intensity, we depict the largest singular value of the downconversion Hamiltonian (A2) in Figure 5. From the analysis of the field correlation function,[32] we know that the coherent contribution of pairs of entangled photons scales as $\sinh(r_k)\cosh(r_k)$, and the incoherent autocorrelation contribution of uncorrelated photons as $\sinh^2(r_k)$. At low pump intensities, $r_k \ll 1$, we can neglect the latter contribution, and approximate the former as $\sinh(r_k)\cosh(r_k) \approx r_k$. This regime is described by the entangled twin photon state,[25] and its contribution is plotted as a dashed line in Figure 5. The four-point correlation function of twin photons scales linearly in the pump intensity,[15] and the crossover of the intensity scaling is commonly regarded as a crossover to a "classical" high intensity regime.[16] However, as pointed out in Ref. 32, this crossover which occurs for $\alpha \simeq 0.002$ in Figure 5 does not coincide with the crossover in the behavior of the four-point correlation function which occurs when the red and blue lines are of similar strength at $\alpha \simeq 0.01$. This can clearly be seen in Figure 4, where panels (a) and (b) look virtually identical, even though only panel (a) can be described by the twin state. In panel (c), the lower peaks become notably stronger with respect to the other resonances, and at much higher amplitudes α [panel (d)], the incoherent contributions finally dominate.

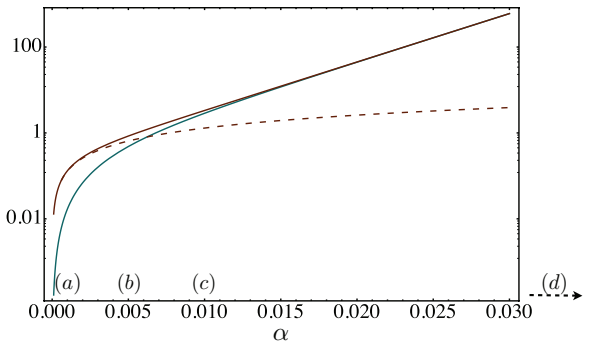

FIG. 5. The largest singular value r_1 of the decomposition of the light interaction Hamiltonian (A2) is plotted vs the pump amplitude α. Red: the coherent contribution $\cosh(r_1)\sinh(r_1)$, blue: the incoherent contribution $\sinh^2(r_1)$. The linear plot (corresponding to the contribution of the twin photon state) is shown as a dashed line. The parameters of the various panels of Figure 4 are marked on the α-axis. This plot illustrates the crossover from twin photons to squeezed light.

IV. SIMULATION OF RAMAN SIGNALS

Using the same squeezed light model described in the Appendix, we have simulated the Raman pathways [diagrams (c) and (d) of Figure 2] in a model system with a single vibrational state with energy $g' = 200\ \mathrm{cm}^{-1}$, and one excited electronic state at $e = 16\,000\ \mathrm{cm}^{-1}$. Each single-photon transition is far off-resonant, which allows us to safely neglect linear processes. But the Raman contributions are nevertheless present in a resonant situation.

Equations (5) and (6) contain contributions with distinct dependence on the time delay δt: one part which decays rapidly with the electronic lifetime γ_e, and a second one which decays more slowly with the vibrational lifetime γ_g. This second part oscillates with $\omega_b - \omega_a - \omega_{g'g}$, and by properly choosing the entangled beam parameters, it should be possible to observe the vibrational coherence $\omega_{g'g}$ in the signal (1).

In Figure 6 we demonstrate this behavior for our model system. We plot Eqs. (5) and (6) vs. the time delay δt for fixed control parameters of the entangled beams in panel (a) [Eqs. (3) and (4) decay almost instantaneously on the time scales shown here]. The signal decays exponentially with the lifetime γ_g, and shows pronounced oscillations. To analyze these oscillations, we depict the Fourier transform of the time signal in panel (b), given by

$$\tilde{S}(\Gamma;\Omega) = \int d\delta t\ e^{i\Omega\delta t}(S_c(\Gamma;\delta t) + S_d(\Gamma;\delta t)). \tag{9}$$

The Fourier transform $\tilde{S}$ of the time signal shows a pronounced peak around $\Omega = 200\ \mathrm{cm}^{-1}$. For an entanglement time of 10 fs, an additional peak at $\Omega = 400\ \mathrm{cm}^{-1}$ can be observed as well. For shorter entanglement times (red plots), the oscillations are a lot more pronounced. This can be explained with the fact that these correspond to larger bandwidths of the individual beams. Hence, each beam is shorter in time, and we obtain better time resolution, whereas the oscillations are washed out for shorter bandwidths. Similar signals can be obtained with ultrafast pulses as well. However, with entangled photons one can use much lower pump intensities as pointed out in the introduction. The field correlation functions [(A13)–(A16)] have contributions $f_{1/2}$ corresponding to the coherent interaction of entangled photon pairs, and scale linearly in the pump intensity for weak pumps.

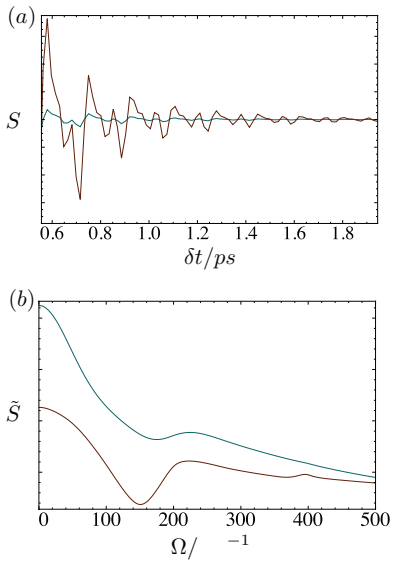

FIG. 6. (a) The Raman signal, Eqs. (5) and (6), is plotted vs. the time delay δt. The entangled beams are created by a pump pulse with width $\sigma_p = 20\ \mathrm{cm}^{-1}$, and entanglement times 100 fs (blue) and 50 fs (red). We further chose $\omega_1 = \omega_2 = \omega = 11\,000\ \mathrm{cm}^{-1}$. The intensity is plotted in arbitrary units, which are not shown. (b) The absolute value of the Fourier transform of the signals (a) [Eq. (9)] with respect to the time delay δt.

V. TRANSITION-AMPLITUDE (KRAMERS-HEISENBERG) FORM FOR TWO-PHOTON SIGNALS

The nonlinear response functions of matter caused by the interaction with a classical light field are often given in terms of susceptibilities. Certain types of optical signals on the other hand may be expressed in terms of transition amplitudes. These are easier to calculate and simplify the interpretation. We shall consider the dissipative signal obtained from Eq. (1) by integrating over the detected frequency[33]

$$S_{\mathrm{dissipative}}(\Gamma) = \int d\omega\ S(\Gamma;\omega,\delta t = 0). \tag{10}$$

To detect the entire dissipated energy, the signal in beam 1 is collected as well. The time delay δt is set to zero to avoid dissipation to the environment during the free evolution. This allows us to combine the field correlation functions into terms $\langle E^\dagger E^\dagger EE\rangle$, where $E = E_1 + E_2$. We therefore eliminate the subscripts in the following.

As shown in Ref. 33, the dissipative signal can be written as the modulus square of *transition amplitudes*,

$$S_{\mathrm{dissipative}}(\Gamma) = \sum_i |T_{ig}|^2, \tag{11}$$

where the summation runs over all the final states i which have a different energy than the initial state g. For the interaction with classical cw-light, the transition amplitudes can be expanded in the number of matter-field interactions,

$$T_{ig}(\omega) = T_{ig}^{(1)}(\omega) + T_{ig}^{(2)}(\omega) + \cdots, \tag{12}$$

where

$$T_{ig}^{(1)}(\omega) = \mu_{gi}, \tag{13}$$

$$T_{ig}^{(2)}(\omega) = \sum_b \frac{\mu_{gb}\mu_{bi}}{\omega - \omega_{bg} + i\gamma}. \tag{14}$$

Since in the derivation of Eqs. (3)–(6) we expanded the density matrix to third order, we can expect the signal to be composed of the following products of transition amplitudes:

$\langle|T^{(2)}|^2\rangle$, $T^{(3)}T^{(1)*}$ + h.c., and $T^{(4)}T^{(0)*}$ + h.c. Equation (4) yields

$$S_b \propto \Im \int\frac{d\omega_a}{2\pi}\int\frac{d\omega_b}{2\pi}\int\frac{d\omega}{2\pi}\langle E^\dagger(\omega)E^\dagger(\omega_a+\omega_b-\omega)E(\omega_b)E(\omega_a)\rangle \times\sum_{e,e',f}\frac{\mu_{ge}\mu_{ef}}{\omega_a-\omega_{eg}+i\gamma_e}\frac{1}{\omega_a+\omega_b-\omega_{fg}+i\gamma_f}\frac{\mu_{fe'}\mu_{e'g}}{\omega-\omega_{e'g}-i\gamma_e}. \tag{15}$$

With the definition of the second-order transition amplitude (14), we obtain

$$S_b \propto \Im \int\frac{d\omega_a}{2\pi}\int\frac{d\omega_b}{2\pi}\int\frac{d\omega'_a}{2\pi}\langle E^\dagger(\omega'_a) \times E^\dagger(\omega_a+\omega_b-\omega'_a)E(\omega_b)E(\omega_a)\rangle \times\sum_f T^{(2)}_{fg}(\omega_a)T^{(2)*}_{fg}(\omega'_a)\frac{1}{\omega_a+\omega_b-\omega_{fg}+i\gamma_f}. \tag{16}$$

Changing to the variable $\omega_p = \omega_a + \omega_b$, we can write the signal more symmetrically,

$$S_b \propto \Im \int\frac{d\omega_p}{2\pi}\int\frac{d\omega_a}{2\pi}\int\frac{d\omega'_a}{2\pi}\langle E^\dagger(\omega'_a)E^\dagger(\omega_p-\omega'_a) \times E(\omega_p-\omega_a)E(\omega_a)\rangle \times\sum_f T^{(2)}_{fg}(\omega_a)T^{(2)*}_{fg}(\omega'_a)\frac{1}{\omega_p-\omega_{fg}+i\gamma_f}. \tag{17}$$

Defining the two-photon transition operator acting on the field space

$$\hat{T}^{(2)}_{fg}(\omega_p;\Gamma) \equiv \int\frac{d\omega}{2\pi}\,\hat{E}(\omega_p-\omega)\hat{E}(\omega)T^{(2)}_{fg}(\omega) \tag{18}$$

(we write $\hat{E}$ to emphasize that the E's are operators) we can write

$$S_b \propto \Im \int\frac{d\omega_p}{2\pi}\,\sum_f\langle|\hat{T}^{(2)}(\omega_p;\Gamma)|^2\rangle\frac{1}{\omega_p-\omega_{fg}+i\gamma_f}. \tag{19}$$

This allows us to take the imaginary value in the limit of small dephasing,

$$\Im\frac{1}{\omega_p-\omega_{fg}+i\gamma_f} = \delta(\omega_p-\omega_{fg}), \tag{20}$$

and we arrive at

$$S_b \propto \int\frac{d\omega_a}{2\pi}\int\frac{d\omega'_a}{2\pi}\,\langle E^\dagger(\omega'_a)E^\dagger(\omega_{fg}-\omega'_a)E(\omega_{fg}-\omega_a)E(\omega_a)\rangle \times\sum_f T^{(2)}_{fg}(\omega_a)T^{(2)*}_{fg}(\omega'_a) \tag{21}$$

$$= \sum_f\langle|\hat{T}^{(2)}(\omega_{fg};\Gamma)|^2\rangle. \tag{22}$$

For classical fields, the field operators in Eq. (22) can be replaced by field amplitudes, and the signal factorizes into a product of transition amplitudes. This is not possible for arbitrary quantum fields, since the field expectation value can create correlations between interactions on both sides of diagram (b) of Fig. 2.

Assuming that the field is in a two-photon Fock state, its correlation function factorizes into

$$\langle E^\dagger(\omega'_a)E^\dagger(\omega'_b)E(\omega_b)E(\omega_a)\rangle = \langle E^\dagger(\omega'_a)E^\dagger(\omega'_b)\rangle\langle E(\omega_b)E(\omega_a)\rangle. \tag{23}$$

This allows us to define the combined matter-field transition amplitude

$$\tilde{T}^{(2)}_{fg}(\omega_{fg};\Gamma) \equiv \int\frac{d\omega}{2\pi}\,\langle E(\omega_{fg}-\omega)E(\omega)\rangle T^{(2)}_{fg}(\omega), \tag{24}$$

where Γ denotes the control parameters of the quantum light, and the signal can be finally recast as

$$S_b \propto \sum_f\left|\tilde{T}^{(2)}_{fg}(\omega_{fg};\Gamma)\right|^2. \tag{25}$$

Diagram (d) of Fig. 2 yields in close analogy

$$S_d \propto \sum_{g'}\left\langle\left|\hat{T}^{(2)}_{g'g}(\omega_{g'g};\Gamma)\right|^2\right\rangle, \tag{26}$$

with the transition amplitude operator

$$\hat{T}^{(2)}_{g'g}(\omega_-;\Gamma) = \int\frac{d\omega}{2\pi}\sum_e\mu_{ge}\frac{E^\dagger(\omega_- -\omega)E(\omega)}{\omega-\omega_{eg}+i\gamma_e}\mu_{eg'}. \tag{27}$$

Equations (3) and (5) describe parametric processes, in which the system evolves $g \to g$. No energy is exchanged with the light field, and the diagrams do not contribute to the dissipative signal (10).

VI. TWO-PHOTON COINCIDENCE: RAMSEY FRINGES

A. Classical Ramsey fringes

Ramsey interferometry has long been used as a time-domain technique for measuring frequencies of atomic transitions with remarkably high precision.[36,37] The technique does not use light pulses. Instead, an atomic beam passes through two cavities with strong fields. These effectively act as pulses with durations given by the transit time through the cavities. An interference fringe is created by varying the delay between the two cavities. The excited state population is measured at the end. The physics is identical to what can be obtained by two pulses and variable delay and fluorescence detection. It can thus be described by transition amplitudes and similar diagrams to what we used for the dissipative signals. In this section we recast the Ramsey signal using our approach and derive expressions that can be used to study pulse shaping, and can be easily extended to include more pulses. We consider both single photon and two photon signals.

As described above, in conventional Ramsey experiments, an ensemble of two-level atoms with ground states $\{|g_i\rangle\}$ and excited states $\{|e_i\rangle\}$ is irradiated by two temporally separated pulses E_1 and E_2 with a relative time delay δt, and the fluorescence is recorded [see Figure 7]. This is proportional to the excited state population

$$S_{\text{classical}}(t;\Gamma) = \text{tr}\left\{\mathcal{T}|e_i(t)\rangle\langle e_i(t)|\exp\left[-\frac{i}{\hbar}\int_{t_0}^t d\tau\,H_-(\tau)\right]\varrho(t_0)\right\}. \tag{28}$$

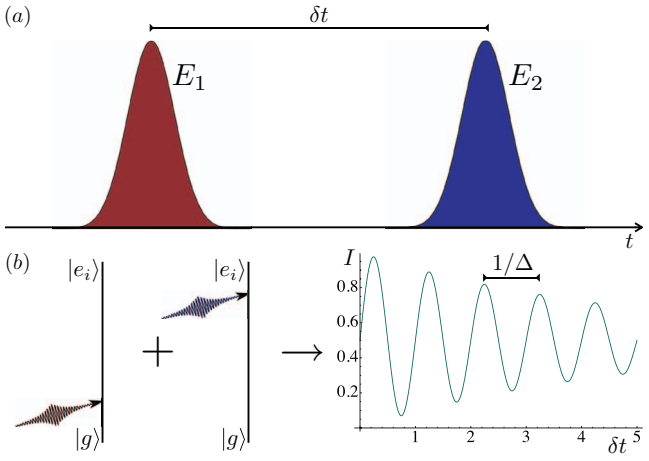

FIG. 7. (a) Pulse sequence for a classical Ramsey experiment. (b) The interference between the excitation of either of the two beams creates the oscillations when plotted vs. the time delay.

This signal is given by four terms depicted in Figure 8. We illustrate the evaluation by considering diagram (b) in detail. It reads

$$S_{\text{classical(b)}} = \int^t d\tau_1 \int^t d\tau_1' \, \langle g|V(\tau_1'+\delta t)|e_i(t)\rangle\langle e_i(t)|V(\tau_1)|g\rangle \times \langle E_2^\dagger(\tau_1'+\tau)E(\tau_1)\rangle. \tag{29}$$

We write the frequency decomposition of the field correlation function as

$$\langle E_2^\dagger(\tau_1'+\delta t)E(\tau_1)\rangle = \int \frac{d\omega_a'}{2\pi}\int \frac{d\omega_a}{2\pi} e^{i\omega_a'(\tau_1'+\delta t)-i\omega_a\tau_1}\langle E_2^\dagger(\omega_a')E_1(\omega_a)\rangle, \tag{30}$$

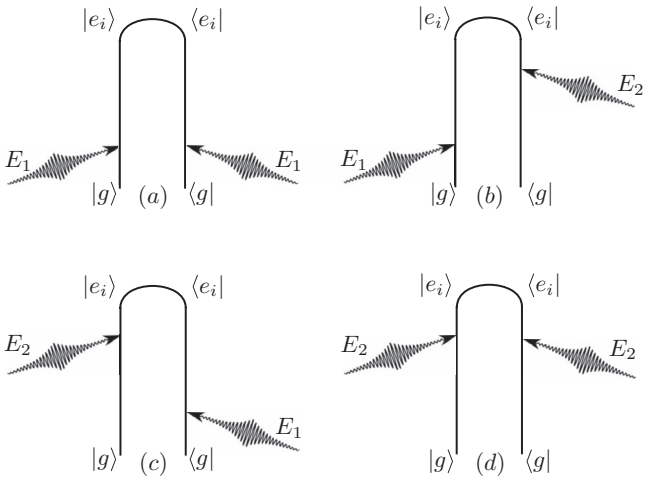

FIG. 8. Pathways of Eq. (28).

and change to the loop times $s_1 = t - \tau_1$ and $s_2 = t - \tau_1'$. We obtain

$$S_{\text{classical(b)}} = \int \frac{d\omega_a'}{2\pi}\int \frac{d\omega_a}{2\pi}\langle E_2^\dagger(\omega_a')E_1(\omega_a)\rangle e^{i(\omega_a'-\omega_a)t} \times \frac{\mu_{ge}}{\omega_a-\omega_{e_ig}+i\eta}\frac{\mu_{eg}e^{i(\omega_a'-\omega_{e_ig})\delta t}}{\omega_a'-\omega_{e_ig}-i\eta}, \tag{31}$$

where we introduced the infinitesimal factor η. When the bandwidth of the two fields is much smaller than the inverse time delay, we can approximate the two-point correlation function by

$$\langle E_2^\dagger(\omega_a')E_1(\omega_a)\rangle \approx E_2^* E_1 \delta(\omega_a'-\omega_2)\delta(\omega_a-\omega_1). \tag{32}$$

The four diagrams can then be combined into the modulus square of a transition amplitude that has two interfering paths,

$$S = |T_{eg}(t;E_1)+T_{eg}(t;E_2)|^2, \tag{33}$$

with

$$T_{eg}(t;E_1) = \frac{\mu_{ge}e^{-i\omega_{eg}t}}{\omega_1-\omega_{eg}+i\eta}, \tag{34}$$

$$T_{eg}(t;E_2) = \frac{\mu_{ge}e^{-i\omega_{eg}t}}{\omega_2-\omega_{eg}+i\eta}e^{i(\omega_2-\omega_{eg})\delta t}. \tag{35}$$

By varying δt the signal oscillates at the frequency $\Delta = \omega_2 - \omega_{eg}$, which is called the detuning. These are the Ramsey fringes which measure ω_{eg} with high resolution.

B. Ramsey fringes with squeezed light

In their extension to squeezed light, Qu and Agarwal[30] defined the fluorescence coincidence as their observable. The doubly excited states are excited by the interaction with two entangled beams. Diagrams (b) and (c) of Figure 8 vanish for squeezed beams, since $\langle E\rangle = 0$ for a squeezed vacuum state. However, $\langle E^2\rangle \neq 0$, and the absorption of pairs of photons from each beam can give rise to similar interference fringes, as we will rederive using our superoperator formalism. This may be advantageous if one were to investigate a dipole-forbidden transition, which can be accessed through a two-photon process.

The photon coincidence signal is proportional to the population of doubly excited states

$$S(t;\Gamma) = \text{tr}\left\{\mathcal{T}|e_i(t),e_j(t)\rangle\langle e_i(t),e_j(t)| \times \exp\left[-\frac{i}{\hbar}\int_{t_0}^t d\tau H_-(\tau)\right]\varrho(t_0)\right\}. \tag{36}$$

To leading order, the signal is given by

$$S(t;\Gamma) = \left(-\frac{i}{\hbar}\right)^4 \int^t d\tau_2 \int^{\tau_2} d\tau_1 \int^t d\tau_2' \int^{\tau_2'} d\tau_1' \times \langle V(\tau_1')V(\tau_2')|e_1e_2(t)\rangle\langle e_1e_2(t)|V^\dagger(\tau_2)V^\dagger(\tau_1)\rangle \times \langle E^\dagger(\tau_1')E^\dagger(\tau_2')E(\tau_2)E(\tau_1)\rangle, \tag{37}$$

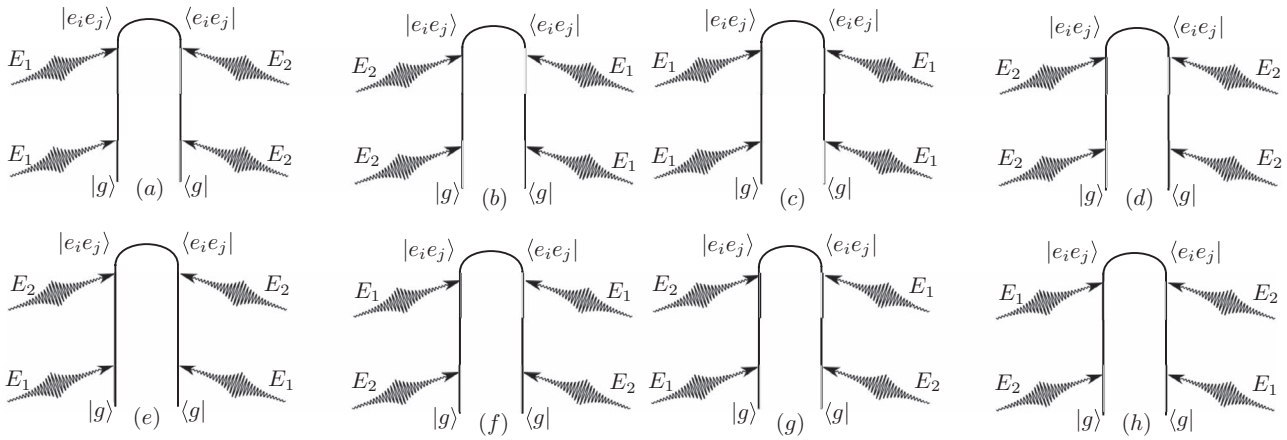

FIG. 9. Pathways of Eq. (36).

where $E(\tau) = E_1(\tau) + E_2(\tau)$. Equation (37) generalizes the results of Ref. 30: it is valid for arbitrary kinds of light—not limited to square pulses or squeezed photons—and for exciton systems with non-vanishing dipole interactions. The loop diagrams corresponding to this expression are depicted in Figure 9. Because of the time delay δt between the two fields 1 and 2, we show each combination of fields separately. Diagrams (a) and (b) are responsible for the higher resolution of the Ramsey fringes compared to classical light, while the other diagrams reduce the visibility of the fringes. Since we assume a finite time delay between the two fields, we can neglect diagrams (f)–(h). Furthermore, diagrams (a) and (b) are complex conjugates, such that we only need to calculate one of the two.

C. Entangled two-photon state

We illustrate the derivation of the signal with diagram (a). It reads

$$\begin{aligned} &S_{(a)}(t;\Gamma) \\ &= \left(-\frac{i}{\hbar}\right)^4 \int^t d\tau_2 \int^{\tau_2} d\tau_1 \int^t d\tau_2' \int^{\tau_2'} d\tau_1' \\ &\quad \times \langle V(\tau_1' + \delta t) V(\tau_2' + \delta t) | e_1 e_2(t)\rangle \langle e_1 e_2(t) | V^\dagger(\tau_2) V^\dagger(\tau_1)\rangle \\ &\quad \times \langle E_2^\dagger(\tau_1' + \delta t) E_2^\dagger(\tau_2' + \delta t) E_1(\tau_2) E_1(\tau_1)\rangle. \end{aligned} \tag{38}$$

Carrying out the time integration, we obtain

$$\begin{aligned} S_{(a)}(t;\Gamma) = &\left(-\frac{i}{\hbar}\right)^4 \int \frac{d\omega_a}{2\pi} \int \frac{d\omega_b}{2\pi} \int \frac{d\omega_a'}{2\pi} \int \frac{d\omega_b'}{2\pi} \left(\frac{\mu_{ge_1}\mu_{ge_2}}{\omega_a - \omega_{e_1g} + i\eta} + \frac{\mu_{ge_1}\mu_{ge_2}}{\omega_a - \omega_{e_2g} + i\eta} \right) \\ &\times \left(\frac{\mu_{ge_1}\mu_{ge_2}}{\omega_a' - \omega_{e_1g} - i\eta} + \frac{\mu_{ge_1}\mu_{ge_2}}{\omega_a' - \omega_{e_2g} - i\eta} \right) \\ &\times \frac{e^{i(\omega_a' + \omega_b' - \omega_a - \omega_b)t}}{\omega_a + \omega_b - \omega_{e_1g} - \omega_{e_2g} + i\eta} \frac{e^{i(\omega_a' + \omega_b' - \omega_{e_1g} - \omega_{e_2g})\delta t}}{\omega_a' + \omega_b' - \omega_{e_1g} - \omega_{e_2g} - i\eta} \\ &\times \langle E_2^\dagger(\omega_a') E_2^\dagger(\omega_b')\rangle \langle E_1(\omega_b) E_1(\omega_a)\rangle. \end{aligned} \tag{39}$$

In the following, we consider entangled twin photons created by degenerate type-II downconversion. They are a good low-intensity approximation of the squeezed light model of Sec. VI B, and allow for a analytical evaluation of the integrals. The field correlation function then reads[38]

$$\langle E_i(\omega_b) E_i(\omega_a)\rangle = C(T_i) \mathrm{sinc}\left(\frac{(\omega_{p_i}/2 - \omega_a) T_i}{2} \right) e^{i(\omega_{p_i}/2 - \omega_a)T_i/2}\, 2\pi\delta(\omega_a + \omega_b - \omega_{p_i}), \tag{40}$$

where ω_{p_i} denotes the pump frequency of field i, T_i its entanglement time, and $C(T_i)$ a normalization constant. In time domain, this correlation function corresponds to square pulses. This yields

$$\begin{aligned} S_{(a)}(t;\Gamma) = &\left(-\frac{i}{\hbar}\right)^4 \int\frac{d\omega_a}{2\pi}\int\frac{d\omega_a'}{2\pi}\left(\frac{\mu_{ge_1}\mu_{ge_2}}{\omega_a-\omega_{e_1g}+i\eta}+\frac{\mu_{ge_1}\mu_{ge_2}}{\omega_a-\omega_{e_2g}+i\eta}\right)\\ &\times\left(\frac{\mu_{ge_1}\mu_{ge_2}}{\omega_a'-\omega_{e_1g}-i\eta}+\frac{\mu_{ge_1}\mu_{ge_2}}{\omega_a'-\omega_{e_2g}-i\eta}\right)\\ &\times\frac{e^{i(\omega_{p_2}-\omega_{p_1})t}}{\omega_{p_1}-\omega_{e_1g}-\omega_{e_2g}+i\eta}\frac{1}{\omega_{p_2}-\omega_{e_1g}-\omega_{e_2g}-i\eta}e^{i(\omega_{p_2}-\omega_{e_1g}-\omega_{e_2g})\delta t}\\ &\times C(T_1)C(T_2)\mathrm{sinc}\left(\frac{(\omega_{p_1}/2-\omega_a)T_1}{2}\right)e^{i(\omega_{p_1}/2-\omega_a)T_1/2}\\ &\times\mathrm{sinc}\left(\frac{(\omega_{p_2}/2-\omega_a')T_2}{2}\right)e^{-i(\omega_{p_2}/2-\omega_a')T_2/2}. \end{aligned} \tag{41}$$

The ω_a-integration can be closed at $-i\infty$, and the ω_a'-integration at $+i\infty$, resulting in

$$\begin{aligned} S_{(a)}(t;\Gamma) = &\left(-\frac{i}{\hbar}\right)^4 C(T_1)C(T_2)\frac{\mu_{ge_1}\mu_{ge_2}}{\omega_{p_1}-\omega_{e_1g}-\omega_{e_2g}+i\eta}\frac{\mu_{ge_1}\mu_{ge_2}}{\omega_{p_2}-\omega_{e_1g}-\omega_{e_2g}-i\eta}e^{i(\omega_{p_2}-\omega_{e_1g}-\omega_{e_2g})\delta t}\\ &\times\left(\mathrm{sinc}\left(\frac{(\omega_{p_1}/2-\omega_{e_1g})T_1}{2}\right)e^{i(\omega_{p_1}/2-\omega_{e_1g})T_1/2}+\mathrm{sinc}\left(\frac{(\omega_{p_1}/2-\omega_{e_2g})T_1}{2}\right)e^{i(\omega_{p_1}/2-\omega_{e_2g})T_1/2}\right)\\ &\times\left(\mathrm{sinc}\left(\frac{(\omega_{e_1g}-\omega_{p_2}/2)T_2}{2}\right)e^{i(\omega_{e_1g}-\omega_{p_2}/2)T_2/2}+\mathrm{sinc}\left(\frac{(\omega_{e_2g}-\omega_{p_2}/2)T_2}{2}\right)e^{i(\omega_{e_2g}-\omega_{p_2}/2)T_2/2}\right), \end{aligned} \tag{42}$$

where we neglected the infinitesimal imaginary factor $\pm i\eta$ in the last two lines.

For identical atoms in Eq. (42), we observe that it oscillates with $2\Delta\delta t$ as shown in Ref. 30. This is however only true for cw-pumped entangled photons. In the general result in Eq. (39), we can see that pulse envelopes affect the oscillations. Furthermore, the signal depends on two different transition frequencies ω_{e_1g} and ω_{e_2g}, which need not be identical.

Similarly, we obtain

$$\begin{aligned} S_{(c)}(t;\Gamma) = &\left(-\frac{i}{\hbar}\right)^4 C^2(T_1)\frac{\mu_{ge_1}^2\mu_{ge_2}^2}{(\omega_{p_1}-\omega_{e_1g}-\omega_{e_2g})^2+\eta^2}\\ &\times\left|\mathrm{sinc}\left(\frac{(\omega_{p_1}/2-\omega_{e_1g})T_1}{2}\right)e^{i(\omega_{p_1}/2-\omega_{e_1g})T_1/2}+\mathrm{sinc}\left(\frac{(\omega_{p_1}/2-\omega_{e_2g})T_1}{2}\right)e^{i(\omega_{p_1}/2-\omega_{e_2g})T_1/2}\right|^2, \end{aligned} \tag{43}$$

$$\begin{aligned} S_{(d)}(t;\Gamma) = &\left(-\frac{i}{\hbar}\right)^4 C^2(T_2)\frac{\mu_{ge_1}^2\mu_{ge_2}^2}{(\omega_{p_2}-\omega_{e_1g}-\omega_{e_2g})^2+\eta^2}\\ &\times\left|\mathrm{sinc}\left(\frac{(\omega_{p_2}/2-\omega_{e_1g})T_2}{2}\right)e^{i(\omega_{p_2}/2-\omega_{e_1g})T_2/2}+\mathrm{sinc}\left(\frac{(\omega_{p_2}/2-\omega_{e_2g})T_2}{2}\right)e^{i(\omega_{p_2}/2-\omega_{e_2g})T_2/2}\right|^2, \end{aligned} \tag{44}$$

which simply consist of the transition amplitude squares for the absorption of the two photons. This allows us to combine Eqs. (42)–(44) into a single transition amplitude squared,

$$S_{(a)-(d)}(t;\Gamma) = |T_1(t;\Gamma)+T_2(t;\Gamma)|^2, \tag{45}$$

with

$$\begin{aligned} T_1(t;\Gamma) = &\left(-\frac{i}{\hbar}\right)^2 C(T_1)\frac{\mu_{ge_1}\mu_{ge_2}e^{-i\omega_{p_1}t}}{\omega_{p_1}-\omega_{e_1g}-\omega_{e_2g}+i\eta}\\ &\times\left(\mathrm{sinc}\left(\frac{(\omega_{p_1}/2-\omega_{e_1g})T_1}{2}\right)e^{i(\omega_{p_1}/2-\omega_{e_1g})T_1/2}+\mathrm{sinc}\left(\frac{(\omega_{p_1}/2-\omega_{e_2g})T_1}{2}\right)e^{i(\omega_{p_1}/2-\omega_{e_2g})T_1/2}\right), \end{aligned} \tag{46}$$

$$\begin{aligned} T_2(t;\Gamma) = &\left(-\frac{i}{\hbar}\right)^2 C(T_2)\frac{\mu_{ge_1}\mu_{ge_2}e^{-i\omega_{p_2}t}}{\omega_{p_2}-\omega_{e_1g}-\omega_{e_2g}+i\eta}e^{i(\omega_{p_2}-\omega_{e_1g}-\omega_{e_2g})\delta t}\\ &\times\left(\mathrm{sinc}\left(\frac{(\omega_{p_2}/2-\omega_{e_1g})T_2}{2}\right)e^{i(\omega_{p_2}/2-\omega_{e_1g})T_2/2}+\mathrm{sinc}\left(\frac{(\omega_{p_2}/2-\omega_{e_2g})T_2}{2}\right)e^{i(\omega_{p_2}/2-\omega_{e_2g})T_2/2}\right). \end{aligned} \tag{47}$$

Besides, diagram (e) yields

$$S_{(e)}(t;\Gamma) = \left(-\frac{i}{\hbar}\right)^4 \int\frac{d\omega_a}{2\pi}\int\frac{d\omega_b}{2\pi}\int\frac{d\omega'_a}{2\pi}\int\frac{d\omega'_b}{2\pi}\frac{e^{i(\omega'_a+\omega'_b-\omega_a-\omega_b)t}}{\omega_a+\omega_b-\omega_{e_1g}-\omega_{e_2g}+i\eta}\frac{\mu^2_{ge_1}\mu^2_{ge_2}}{\omega'_a+\omega'_b-\omega_{e_1g}-\omega_{e_2g}-i\eta}$$
$$\times\left(\frac{e^{-i\omega_{e_1g}\delta t}}{\omega_a-\omega_{e_1g}+i\eta}+\frac{e^{-i\omega_{e_2g}\delta t}}{\omega_a-\omega_{e_2g}+i\eta}\right)\left(\frac{e^{i\omega_{e_1g}\delta t}}{\omega'_a-\omega_{e_1g}-i\eta}+\frac{e^{i\omega_{e_2g}\delta t}}{\omega'_a-\omega_{e_2g}-i\eta}\right)$$
$$\times\langle E_2^\dagger(\omega'_b)E_2(\omega_b)\rangle\langle E_1^\dagger(\omega'_a)E_1(\omega_a)\rangle e^{i(\omega_b-\omega'_b)\delta t}, \tag{48}$$

with the two-point field correlation function

$$\langle E_i^\dagger(\omega'_a)E_i(\omega_a)\rangle = C^2(T_i)\mathrm{sinc}^2\left(\frac{(\omega_a-\omega_{p_i}/2)T_i}{2}\right)2\pi\delta(\omega_a-\omega'_a). \tag{49}$$

Finally we obtain

$$S_{(e)}(t;\Gamma) = \int\frac{d\omega_a}{2\pi}\int\frac{d\omega_b}{2\pi}\left|T_3(\omega_a,\omega_b,t;\Gamma)\right|^2, \tag{50}$$

with

$$T_3(\omega_a,\omega_b,t;\Gamma) = \left(-\frac{i}{\hbar}\right)^2\frac{C(T_1)C(T_2)\mathrm{sinc}\left(\frac{(\omega_a-\omega_{p_1}/2)T_1}{2}\right)\mathrm{sinc}\left(\frac{(\omega_b-\omega_{p_2}/2)T_2}{2}\right)}{\omega_a+\omega_b-\omega_{e_1g}-\omega_{e_2g}+i\eta}$$
$$\times\left(\frac{e^{-i\omega_{e_1g}\delta t}}{\omega_a-\omega_{e_1g}+i\eta}+\frac{e^{-i\omega_{e_2g}\delta t}}{\omega_a-\omega_{e_2g}+i\eta}\right). \tag{51}$$

In contrast to Eq. (42), Eq. (50) does not depend on the detuning of the pump pulse with respect to the doubly excited state energy, but instead on the energy difference between the two transition energies ω_{e_1g} and ω_{e_2g}. If the two energies are identical as was assumed in Ref. 30, it only creates a constant background, which reduces the visibility of the fringes.

To conclude, the second-order diagrams of Figure 8 which give rise to oscillations with the frequency $\Delta = \omega_2 - \omega_{eg}$ vanish for the squeezed vacuum state as well as for the twin photon state. But the fourth order diagrams of Figure 9 give rise to a different kind of Ramsey oscillations with the frequency 2Δ (provided $e_1 = e_2$).

VII. CONCLUSIONS

We have studied the frequency-resolved transmission signal of entangled beams interacting with a three-level model system. The nonclassical bandwidth features of the beams can be used to enhance otherwise weak or hidden signals, as was demonstrated by comparing the signal to a transmission signal of a classical laser pulse. As the intensity of the entangled beams is increased, entangled pairs start to overlap, and the nonclassical features of the signal are degraded. For very high intensities, the signal looks similar to its classical counterpart.

The introduction of a delay stage in one of the beams can be used to monitor vibrational resonances. This effect is not caused by nonclassical bandwidth properties, and can be seen with classical light as well. However, the linear scaling at low intensities allows for the use of very low intensities, thus minimizing damage to the sample.

We further expressed the frequency-integrated signal in terms of transition amplitudes, extending known results for the interaction with classical light. Finally, we have derived the superoperator expressions for the photon counting signal.

ACKNOWLEDGMENTS

We gratefully acknowledge the support of the National Science Foundation through Grant No. CHE-1058791, and the Chemical Sciences, Geosciences and Biosciences Division, Office of Basic Energy Sciences, Office of Science, US Department of Energy.

APPENDIX: THE FIELD CORRELATION FUNCTION FOR SQUEEZED LIGHT

The squeezed state of the field is given by interaction of the downconversion Hamiltonian acting on the vacuum,[39,40]

$$|\psi_f\rangle = U_{PDC}|0\rangle, \tag{A1}$$

where

$$U_{PDC} = \otimes_k \exp[r_k A_k^\dagger B_k^\dagger - \text{h.c.}] \tag{A2}$$

is given by the tensor product of two-mode squeezers in each Schmidt mode k, which are defined by the phase-matching conditions during the down-conversion process. The action of the unitary operator (A2) on the creation and annihilation operators is given by input-output relations. We need to evaluate the four-point correlation functions of Eqs. (3)–(6); the first line of Eq. (3) is given by

$$\langle E_2^\dagger(\omega'_a)E_1^\dagger(\omega'_b)E_2(\omega_b)E_1(\omega_a)\rangle$$
$$= \langle\psi_f|E_2^\dagger(\omega'_a)E_1^\dagger(\omega'_b)E_2(\omega_b)E_1(\omega_a)|\psi_f\rangle, \tag{A3}$$

which results in Ref. 32,

$$\langle E_2^\dagger(\omega_a')E_1^\dagger(\omega_b')E_2(\omega_b)E_1(\omega_a)\rangle = f_2^*(\omega_a',\omega_b')f_1(\omega_a,\omega_b) + g_2(\omega_a,\omega_b')g_1(\omega_b,\omega_a'), \quad \text{(A4)}$$

where

$$f_1^*(\omega,\omega') = \sum_k \sinh(r_k)\cosh(r_k)\psi_k(\omega)\phi_k(\omega'), \quad \text{(A5)}$$

$$f_2^*(\omega,\omega') = \sum_k \sinh(r_k)\cosh(r_k)\phi_k(\omega)\psi_k(\omega'), \quad \text{(A6)}$$

$$g_1(\omega,\omega') = \sum_k \sinh^2(r_k)\psi_k(\omega)\psi_k^*(\omega'), \quad \text{(A7)}$$

$$g_2(\omega,\omega') = \sum_k \sinh^2(r_k)\phi_k(\omega)\phi_k^*(\omega'). \quad \text{(A8)}$$

Here, $\{\psi_k\}$ and $\{\phi_k\}$ are the frequency envelopes of the Schmidt modes; they are connected to the operators given above by

$$A_k = \int d\omega_a \psi_k(\omega_a)a(\omega_a) \quad \text{and} \quad B_k = \int d\omega_b \phi_k(\omega_b)b(\omega_b). \quad \text{(A9)}$$

It can be further shown that these envelopes can be approximated by Hermite functions, enabling us to evaluate (A4) analytically. There are no more differences between g_1 and g_2 (or between f_1 and f_2) in this approximation.

Similarly, we obtain

$$\langle E_2^\dagger(\omega_a')E_1^\dagger(\omega_b')E_1(\omega_b)E_2(\omega_a)\rangle = f_2^*(\omega_a'.\omega_b')f_2(\omega_a,\omega_b) + g_2(\omega_a,\omega_a')g_1(\omega_b,\omega_b'), \quad \text{(A10)}$$

$$\langle E_1^\dagger(\omega_a')E_2^\dagger(\omega_b')E_2(\omega_b)E_1(\omega_a)\rangle = f_1^*(\omega_a'.\omega_b')f_1(\omega_a,\omega_b) + g_1(\omega_a,\omega_a')g_2(\omega_b,\omega_b'), \quad \text{(A11)}$$

$$\langle E_1^\dagger(\omega_a')E_2^\dagger(\omega_b')E_1(\omega_b)E_2(\omega_a)\rangle = f_1^*(\omega_a'.\omega_b')f_2(\omega_a,\omega_b) + g_1(\omega_b,\omega_a')g_2(\omega_a,\omega_b'), \quad \text{(A12)}$$

$$\langle E_2^\dagger(\omega_a')E_2(\omega_b')E_1^\dagger(\omega_b)E_1(\omega_a)\rangle = f_2^*(\omega_a',\omega_b)f_1(\omega_a,\omega_b') + g_1(\omega_a,\omega_b)g_2(\omega_a',\omega_b'), \quad \text{(A13)}$$

$$\langle E_2^\dagger(\omega_a')E_1(\omega_b')E_1^\dagger(\omega_b)E_2(\omega_a)\rangle = f_2^*(\omega_a',\omega_b)f_2(\omega_a,\omega_b') + g_2(\omega_a,\omega_a')g_1(\omega_b,\omega_b'), \quad \text{(A14)}$$

$$\langle E_1^\dagger(\omega_a')E_1(\omega_b')E_2^\dagger(\omega_b)E_2(\omega_a)\rangle = f_1^*(\omega_a',\omega_b)f_2(\omega_a,\omega_b') + g_2(\omega_a,\omega_b)g_1(\omega_a',\omega_b'), \quad \text{(A15)}$$

$$\langle E_1^\dagger(\omega_a')E_2(\omega_b')E_2^\dagger(\omega_b)E_1(\omega_a)\rangle = f_1^*(\omega_a'.\omega_b)f_1(\omega_a,\omega_b') + g_1(\omega_a,\omega_a')g_2(\omega_b,\omega_b'). \quad \text{(A16)}$$

[1] S. Mukamel, D. Abramavicius, L. Yang, W. Zhuang, I. V. Schweigert, and D. V. Voronine, Acc. Chem. Res. **42**, 553 (2009).
[2] S. T. Cundiff and S. Mukamel, Phys. Today **66**, 44 (2013).
[3] G. S. Schlau-Cohen, A. Ishizaki, and G. R. Fleming, Chem. Phys. **386**, 1 (2011).
[4] J. Kim, S. Mukamel, and G. D. Scholes, Acc. Chem. Res. **42**, 1375 (2009).
[5] D. Bimberg, C. Lienau, and T. Elsaesser, *NanoScience and Technology* (Springer, Berlin, Heidelberg, 2008), pp. 301–328.
[6] S. Cundiff, A. Bristow, M. Siemens, H. Li, G. Moody, D. Karaiskaj, X. Dai, and T. Zhang, IEEE J. Sel. Top. Quantum Electron. **18**, 318 (2012).
[7] J. C. Petersen, S. Kaiser, N. Dean, A. Simoncig, H. Y. Liu, A. L. Cavalieri, C. Cacho, I. C. E. Turcu, E. Springate, F. Frassetto, L. Poletto, S. S. Dhesi, H. Berger, and A. Cavalleri, Phys. Rev. Lett. **107**, 177402 (2011).
[8] M. Först, R. I. Tobey, S. Wall, H. Bromberger, V. Khanna, A. L. Cavalieri, Y.-D. Chuang, W. S. Lee, R. Moore, W. F. Schlotter, J. J. Turner, O. Krupin, M. Trigo, H. Zheng, J. F. Mitchell, S. S. Dhesi, J. P. Hill, and A. Cavalleri, Phys. Rev. B **84**, 241104(R) (2011).
[9] J. Orenstein, Phys. Today **65**, 44–50 (2012).
[10] M. Celebrano, P. Kukura, A. Renn, and V. Sandoghar, Nat. Photonics **5**, 95 (2011).
[11] A. Gaiduk, M. Yorulmaz, P. V. Ruijgrok, and M. Orrit, Science **330**, 353 (2010).
[12] S. Chong, W. Min, and X. S. Xie, J. Phys. Chem. Lett. **1**, 3316 (2010).
[13] A. M. Steinberg, P. G. Kwiat, and R. Y. Chiao, Phys. Rev. Lett. **68**, 2421 (1992).
[14] A. N. Boto, P. Kok, D. S. Abrams, S. L. Braunstein, C. P. Williams, and J. P. Dowling, Phys. Rev. Lett. **85**, 2733 (2000).
[15] J. Javanainen and P. L. Gould, Phys. Rev. A **41**, 5088 (1990).
[16] D.-I. Lee and T. Goodson, J. Phys. Chem. B **110**, 25582 (2006).
[17] A. R. Guzman, M. R. Harpham, O. Suzer, M. M. Haley, and T. G. Goodson, J. Am. Chem. Soc. **132**, 7840 (2010).
[18] L. Upton, M. Harpham, O. Suzer, M. Richter, S. Mukamel, and T. Goodson, J. Phys. Chem. Lett. **4**, 2046 (2013).
[19] O. Roslyak, C. A. Marx, and S. Mukamel, Phys. Rev. A **79**, 033832 (2009).
[20] O. Roslyak and S. Mukamel, Phys. Rev. A **79**, 063409 (2009).
[21] F. Schlawin, K. E. Dorfman, B. P. Fingerhut, and S. Mukamel, Phys. Rev. A **86**, 023851 (2012).
[22] H. Oka, J. Chem. Phys. **134**, 124313 (2011).
[23] H. Oka, J. Chem. Phys. **135**, 164304 (2011).
[24] F. Schlawin, K. E. Dorfman, B. P. Fingerhut, and S. Mukamel, Nat. Commun. **4**, 1782 (2013).
[25] H.-B. Fei, B. M. Jost, S. Popescu, B. E. A. Saleh, and M. C. Teich, Phys. Rev. Lett. **78**, 1679 (1997).
[26] B. E. A. Saleh, B. M. Jost, H.-B. Fei, and M. C. Teich, Phys. Rev. Lett. **80**, 3483 (1998).
[27] S. Mukamel and M. Richter, Phys. Rev. A **83**, 013815 (2011).
[28] G. A. Lott, A. Perdomo-Ortiz, J. K. Utterback, J. R. Widom, A. Aspuru-Guzik, and A. H. Marcus, Proc. Natl. Acad. Sci. U.S.A. **108**, 16521 (2011).
[29] R. Hildner, D. Brinks, and N. F. van Hulst, Nat. Phys. **7**, 172 (2011).
[30] K. Qu and G. S. Agarwal, Opt. Lett. **38**, 2563 (2013).
[31] M. Richter and S. Mukamel, Phys. Rev. A **82**, 013820 (2010).
[32] F. Schlawin and S. Mukamel, J. Phys. B **46**, 175502 (2013).
[33] S. Mukamel, and S. Rahav, in *Advances in Atomic, Molecular, and Optical Physics*, edited by P. B. E. Arimondo, and C. Lin (Academic Press, 2010), Vol. 59, pp. 223–263.
[34] A. S. Davydov, Sov. Phys. Usp. **7**, 145 (1964).
[35] M. Khalil and A. Tokmakoff, Chem. Phys. **266**, 213 (2001).
[36] C. Cohen-Tannoudji and D. Guéry-Odelin, *Advances In Atomic Physics: An Overview* (World Scientific Publishing Company, Singapore, 2011).
[37] N. F. Ramsey, Phys. Rev. **78**, 695 (1950).
[38] J. Peřina, B. E. A. Saleh, and M. C. Teich, Phys. Rev. A **57**, 3972 (1998).
[39] A. Christ, K. Laiho, A. Eckstein, K. N. Cassemiro, and C. Silberhorn, New J. Phys. **13**, 033027 (2011).
[40] A. Christ, B. Brecht, W. Mauerer, and C. Silberhorn, New J. Phys. **15**, 053038 (2013).